Department of Applied Mechanics

Application of the random choice method to shallow water equations

Petteri Peltonen

Aalto University | SCIENCE + TECHNOLOGY | REPORT

Aalto University publication series
SCIENCE + **TECHNOLOGY** 17/2015

Application of the random choice method to shallow water equations

Petteri Peltonen

Aalto University
School of Engineering
Department of Applied Mechanics
Marine Technology

Aalto University publication series
SCIENCE + **TECHNOLOGY** 17/2015

ISBN 978-952-60-6580-9 (pdf)
ISSN-L 1799-4896
ISSN 1799-4896 (printed)
ISSN 1799-490X (pdf)
http://urn.fi/URN:ISBN:978-952-60-6580-9

Unigrafia Oy
Helsinki 2015

Finland

Author
Petteri Peltonen

Name of the publication
Application of the random choice method to shallow water equations

Publisher School of Engineering

Unit Department of Applied Mechanics

Series Aalto University publication series SCIENCE + TECHNOLOGY 17/2015

Field of research Marine Technology

Abstract

The Random Choice Method is applied to the one-dimensional shallow water equations with operational splitting to take into account forced domain motion. The Random Choice Method is based on randomly sampling exact Riemann solutions and thus the Riemann solution for the shallow water equations plays a key role in applying the method. The details of the application are presented and the methods accuracy and applicability is discussed through comparison to experimental results as well as literature review. Furthermore, the possible extension of the method to two dimensions is discussed.

Since much of the physics of the flow is neglected in assumptions made in the derivation of the shallow water equations, it is clear that phenomena such as wave breaking and turbulence effects can not be captured with the method. However, the results obtained here show that the method can be applied to solve the shallow water motion under domain excitation, as long as the excitation frequency is relatively low. With higher frequencies of excitation the results show error in the conservation of mass.

Keywords random choice method, shallow water equations, sloshing

ISBN (printed)	**ISBN (pdf)** 978-952-60-6580-9	
ISSN-L 1799-4896	**ISSN (printed)** 1799-4896	**ISSN (pdf)** 1799-490X
Location of publisher Helsinki	**Location of printing** Helsinki	**Year** 2015
Pages 44	**urn** http://urn.fi/URN:ISBN:978-952-60-6580-9	

Preface

This study was carried out in the Marine Hydrodynamics Research Group of the Department of Applied Mechanics at Aalto University during summer and fall of 2015. The aim was to apply the Random Choice Method to solve shallow water motion in an excited domain and to evaluate the accuracy and applicability of the method in the same context. This report is a result of the research group's ongoing research on the simulation of floodwater motion and its effect on ship stability.

I am very grateful to Teemu Manderbacka and Tommi Mikkola for their guidance and for the opportunity to study this subject and to Otto Puolakka for his help in various technical aspects of the work. I also want to thank Professor Timo Siikonen for reviewing the manuscript and providing helpful comments.

Espoo, November 26, 2015,

Petteri Peltonen

Contents

Symbols and abbreviations

Symbols

a_z	source term due to the vertical body force
c	celerity ($c = \sqrt{a_z h}$)
C	Courant number
$\frac{D}{Dt}$	material derivative
E	error
$\mathbf{F}$	vector of fluxes in the conservation form
F_x, F_z	additional body forces exerted on a fluid particle
f_x	source term due to the horizontal body force
f_L, f_R	functions connecting the star region to the initial states in the Riemann problem
g	gravitational acceleration
H	initial water height
h	water height
i	spatial index
k_1, k_2	integers in the van der Corput sequence
n	time level
O	order of error
p	pressure
p_{atm}	atmospheric pressure

$\mathbf{S}$ vector of additional sources

S speed of discontinuity

$T.V.(f)$ total variation of f

t time

Δt temporal step size

$\mathbf{U}$ vector of conservative variables

u horizontal velocity component of the fluid

$\bar{u}$ depth-averaged horizontal velocity of the fluid

$\mathbf{v}$ right eigenvector

$\mathbf{W}$ vector of primitive variables

w vertical velocity component of the fluid

X, Z spatial coordinates in the global coordinate system

x, z spatial coordinates in the fluid coordinate system

Δx spatial step size

Greek alphabet

θ random variable

λ eigenvalue

ϕ roll angle of the domain

φ smooth test function

$\Omega, \dot{\Omega}$ roll angular velocity and acceleration of the domain

Abbreviations

RHS Right-Hand Side

RMC Random Choice Method or Glimm's method

SPH Smoothed Particle Hydrodynamics

VOF Volume Of Fluid

1. Introduction

The numerical solution of free surface gravitational flows has been an interest of engineers and researchers for quite some time. With growing computer capacity and development of the free surface methods it is now possible to simulate free surface engineering problems quite accurately. Some of the frequently used methods for the free surface flows are the Volume of Fluid (VOF) -type [1] surface capturing methods and the meshless Smoothed Particle Hydrodynamics (SPH) methods [2]. However, the accuracy of these methods is achieved with quite substantial amount of computational resources.

When the horizontal length scales of the flow are significantly larger than the vertical length scales, the motion of the fluid can be described with the shallow water equations. Compared to the Navier-Stokes equations, the numerical solution of the shallow water equations can be obtained with much less computational effort while retaining quite good accuracy of the physics of the flow. The solution of the non-linear shallow water equations, especially when hydraulic jumps and dry regions occur, is still not a trivial task.

Many of the numerical schemes used in fluid dynamics rely on either exact or approximate (or linearized [3]) Riemann solvers and that is the case here as well. Often the first order Godunov-type schemes have a tendency to smear the discontinuities whereas some of the more 'standard' high-order schemes may crash in the presence of dry regions or produce high oscillations near the discontinuities.

The Random Choice Method (RMC) used here to solve the shallow water equations in a one-dimensional domain was first introduced by James Glimm in [4] and applied efficiently to the Euler equations by Chorin in [5]. The first applications to the shallow water equations were by Dillingham in [6] and Marshall & Mendez in [7]. Both papers were pub-

lished in the same year. Dillingham coupled the ship motion to the fluid motion and solved shallow water flow on the ship deck and Marshall & Mendez applied the method to the dam break problem, which will also be discussed in this work. Since the results obtained in [6, 7] were quite accurate and the method requires no additional treatment near discontinuities or dry regions, the application of the method is chosen as the topic of the present work.

The second chapter of this work is dedicated to the derivation of the one-dimensional shallow water equations, properties of the equations and to the exact solution of the Riemann problem for shallow water equations, which is a key part of the RCM. The derivation is based on the assumptions of the domain motion made in [8] by Armenio and La Rocca. The solution of the Riemann problem presented in the second chapter is based on the book [9] by Toro and the computer code used in this work to solve the equations is also based on the exact Riemann solver in the same book.

In the third chapter, some details of the RCM and the proof [4] by Glimm are discussed. Additionally, the random sampling procedure of the RCM and the operational splitting technique used to take into account the domain motion is discussed in the third chapter.

The results obtained with the RCM for the dam break problem and shallow water sloshing problem are presented and compared to experimental results in the fourth chapter. In the last chapter the results and the methods applicability are discussed.

2. The shallow water equations

2.1 Derivation and properties

When the horizontal length scale of the flow is much larger than the vertical length scale and viscous effects are negligible, the Navier-Stokes equations can be significantly simplified resulting in the well-known shallow water equations. The assumption that the vertical acceleration of the flow has a negligible effect on the pressure allows the treatment of the vertical pressure gradient as in hydrostatics and the horizontal pressure gradient can be linked to the displacement of the free-surface. Furthermore, by depth-integrating the continuity equation it is possible to remove the vertical velocity component from the equations resulting in a two-dimensional non-linear hyperbolic equation system for an originally three-dimensional domain. In this study the flow field is assumed to be two-dimensional and thus the corresponding shallow water equations are one-dimensional.

Using the notation presented in Figure 2.1, the two dimensional Euler equations are given as

$$\begin{aligned} &\frac{\partial u}{\partial x} + \frac{\partial w}{\partial z} = 0 \\ &\frac{Du}{Dt} + \frac{1}{\rho}\frac{\partial p}{\partial x} = F_x \\ &\frac{Dw}{Dt} + \frac{1}{\rho}\frac{\partial p}{\partial z} = F_z \end{aligned} \tag{2.1}$$

where u and w are the horizontal and vertical velocity components, respectively, p is the pressure and F_x and F_z are additional body forces experienced by a fluid particle with position vector r as in Figure 2.1. Operator D/Dt is the material derivative. If the motion of the domain is restricted to roll only (translation does not affect the derivation of the shallow water

equations), the body forces are given as [8]

$$\begin{aligned} F_x &= -g\sin\phi + 2\Omega w + \dot{\Omega}z + \Omega^2 x \\ F_z &= -g\cos\phi - 2\Omega u - \dot{\Omega}x + \Omega^2 z, \end{aligned} \tag{2.2}$$

where ϕ, Ω and $\dot{\Omega}$ are the roll angle, velocity and acceleration, respectively, and g is the gravitational acceleration.

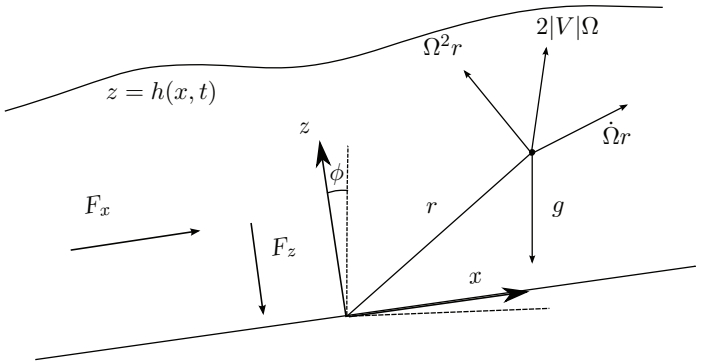

Figure 2.1. The geometry of the shallow water flow. Same notation is used throughout the work.

The derivation of the one-dimensional shallow water equations can be begun by assuming that the vertical component of the fluid acceleration (Dw/Dt) is zero, resulting in an equation for the vertical pressure gradient

$$\frac{1}{\rho}\frac{\partial p}{\partial z} = F_z. \tag{2.3}$$

If the dynamic free-surface boundary condition $p(x,h,t) = p_{atm} = 0$ is applied on the free-surface and Equation (2.3) is integrated with respect to z, the pressure can be expressed as

$$\frac{1}{\rho}p = gh\cos\phi + 2\Omega h\bar{u} + \dot{\Omega}xh - \frac{1}{2}\Omega^2 h^2, \tag{2.4}$$

where the overbar in the velocity denotes the depth-averaged velocity. Here the atmospheric pressure p_{atm} is fixed to zero for convenience. The horizontal pressure gradient is now obtained by differentiating Equation (2.4) with respect to x

$$\frac{1}{\rho}\frac{\partial p}{\partial x} = g\frac{\partial h}{\partial x}\cos\phi + 2\Omega\frac{\partial(h\bar{u})}{\partial x} + \dot{\Omega}h + \dot{\Omega}x\frac{\partial h}{\partial x} - \Omega^2 h\frac{\partial h}{\partial x}. \tag{2.5}$$

Approximating the horizontal Coriolis force as small ($2\Omega w \approx 0$) allows writing of the x-momentum equation as [8]

$$\begin{aligned} &\frac{Du}{Dt} + g\frac{\partial h}{\partial x}\cos\phi + 2\Omega\frac{\partial(h\bar{u})}{\partial x} + \dot{\Omega}h + \dot{\Omega}x\frac{\partial h}{\partial x} - \Omega^2 h\frac{\partial h}{\partial x} \\ &= -g\sin\phi + 2\Omega w + \dot{\Omega}z + \Omega^2 x. \end{aligned} \tag{2.6}$$

Or in a more convenient form

$$\begin{aligned}&\frac{Du}{Dt}+\frac{\partial h}{\partial x}\underbrace{\left(g\cos\phi+2\Omega\bar{u}+\dot{\Omega}x-\Omega^2 h\right)}_{a_z}\\&=\underbrace{\left(-2\Omega h\frac{\partial\bar{u}}{\partial x}-g\sin\phi+\dot{\Omega}(z-h)+\Omega^2 x\right)}_{f_x}.\end{aligned}\tag{2.7}$$

To get rid of the w velocity component the continuity equation is integrated with respect to z between the bottom and the free-surface

$$\begin{aligned}&\int_{z=0}^{z=h}\left(\frac{\partial u}{\partial x}+\frac{\partial w}{\partial z}\right)dz=0\\&\Leftrightarrow w(x,h,t)-w(x,0,t)+\int_0^h\left(\frac{\partial u}{\partial x}dz\right)=0.\end{aligned}\tag{2.8}$$

If the kinematic free-surface condition is applied at the free-surface and the impermeability condition at the bottom, the horizontal velocities can be written as

$$\begin{aligned}w(x,h,t)&=\frac{\partial h}{\partial t}+u(x,h,t)\frac{\partial h}{\partial x}=\frac{\partial h}{\partial t}+\bar{u}\frac{\partial h}{\partial x}\\w(x,0,t)&=u(x,0,t)\frac{\partial h}{\partial x}=\bar{u}\frac{\partial h}{\partial x}.\end{aligned}\tag{2.9}$$

In Equation (2.9), the fact that the depth-averaged velocity component $\bar{u}$ is independent of z was used. For the remaining integral of Equation (2.8) the Leibniz's integral rule is applied

$$\frac{d}{d\theta}\left(\int_{a(\theta)}^{b(\theta)}f(x,\theta)dx\right)=\int_{a(\theta)}^{b(\theta)}\frac{\partial f}{\partial\theta}dx+f(b,\theta)\frac{db}{d\theta}-f(a,\theta)\frac{da}{d\theta}\tag{2.10}$$

or in this case

$$\int_0^h\left(\frac{\partial u}{\partial x}\right)dz=\frac{d}{dx}\left(\int_0^h u dz\right)=\frac{d}{dx}(\bar{u}h).\tag{2.11}$$

Substituting Equations (2.9) and (2.11) to Equation (2.8), the continuity equation without the horizontal velocity component is obtained

$$\begin{aligned}&\frac{\partial h}{\partial t}+\bar{u}\frac{\partial h}{\partial x}-\bar{u}\frac{\partial h}{\partial x}+\frac{\partial(h\bar{u})}{\partial x}=0\\&\Leftrightarrow\frac{\partial h}{\partial t}+\frac{\partial(h\bar{u})}{\partial x}=0.\end{aligned}\tag{2.12}$$

The final form of the one-dimensional shallow water equations is obtained by approximating the material derivative $\frac{Du}{Dt}\approx\frac{\partial\bar{u}}{\partial t}+\bar{u}\frac{\partial\bar{u}}{\partial x}$

$$\begin{aligned}&\frac{\partial h}{\partial t}+\frac{\partial(hu)}{\partial x}=0\\&\frac{\partial u}{\partial t}+u\frac{\partial u}{\partial x}+a_z\frac{\partial h}{\partial x}=f_x.\end{aligned}\tag{2.13}$$

Here the overbars have been dropped from the velocities and the fluid velocities used in the rest of the work are always depth-averaged. Furthermore, the terms a_z and f_x will be treated as locally constant from now on. This is discussed in more detail in Section 3.3.

By expanding the derivative in the continuity equation of (2.13) the system can be written in the primitive form as

$$\mathbf{W}_t + \mathbf{A}(\mathbf{W})\mathbf{W}_x = \mathbf{S}, \tag{2.14}$$

where the lower indices denote differentiation and

$$\mathbf{W} = \begin{bmatrix} h \\ u \end{bmatrix} \quad \mathbf{A}(\mathbf{W}) = \begin{bmatrix} u & h \\ a_z & u \end{bmatrix} \quad \mathbf{S} = \begin{bmatrix} 0 \\ f_x \end{bmatrix}. \tag{2.15}$$

The eigenvalues and the corresponding (right) eigenvectors of the matrix $\mathbf{A}$ are

$$\mathbf{\Lambda} = \begin{bmatrix} u-c & 0 \\ 0 & u+c \end{bmatrix} \quad \mathbf{v^{(1)}} = \begin{bmatrix} 1 \\ -c/h \end{bmatrix} \quad \mathbf{v^{(2)}} = \begin{bmatrix} 1 \\ c/h \end{bmatrix}, \tag{2.16}$$

where c is the celerity $c = \sqrt{a_z h}$.

To define the structure of the shock waves that may occur in solving the the shallow water equations, Equations (2.14) must be written in the conservative form

$$\mathbf{U}_t + \mathbf{F}(\mathbf{U})_x = \mathbf{S}, \tag{2.17}$$

and for a constant a_z

$$\mathbf{U} = \begin{bmatrix} h \\ hu \end{bmatrix} \quad \mathbf{F}(\mathbf{U}) = \begin{bmatrix} hu \\ hu^2 + \frac{1}{2}a_z h^2 \end{bmatrix} \quad \mathbf{S} = \begin{bmatrix} 0 \\ hf_x \end{bmatrix}. \tag{2.18}$$

The Jacobian of the flux vector $\mathbf{F}(\mathbf{U})$ in Equation (2.18) is

$$\tilde{\mathbf{A}} = \frac{\partial \mathbf{F}}{\partial \mathbf{U}} = \begin{bmatrix} 0 & 1 \\ c^2 - u^2 & 2u \end{bmatrix} \tag{2.19}$$

and the eigenstructure $\tilde{\mathbf{A}} = \tilde{\mathbf{R}}\tilde{\mathbf{\Lambda}}\tilde{\mathbf{L}}$ is

$$\tilde{\mathbf{R}} = \begin{bmatrix} 1 & 1 \\ u-c & u+c \end{bmatrix} \quad \tilde{\mathbf{\Lambda}} = \begin{bmatrix} u-c & 0 \\ 0 & u+c \end{bmatrix} \quad \tilde{\mathbf{L}} = \begin{bmatrix} \frac{u+c}{2c} & -\frac{1}{2c} \\ -\frac{u-c}{2c} & \frac{1}{2c} \end{bmatrix}. \tag{2.20}$$

It should be noted that the tilde notation does not denote linearization of the Jacobian in this context.

2.2 Riemann problem

The Riemann problem for a non-linear hyperbolic system is defined as initial value problem

$$\begin{aligned} &\mathbf{U}_t + \mathbf{F}(\mathbf{U})_x = 0 \\ &\mathbf{U}(x, t=0) = \begin{cases} \mathbf{U}_L & \text{if } x < 0 \\ \mathbf{U}_R & \text{if } x > 0 \end{cases}, \end{aligned} \tag{2.21}$$

where $\mathbf{U}_L$ and $\mathbf{U}_R$ denote the initial values on the left and right sides of the discontinuity.

As mentioned before, Equations (2.14) form a hyperbolic system with each eigenvalue (charasteristic speed) corresponding to a wave family as in Figure 2.2. Due to non-linearity of the system, the waves can be either shock waves (bores) or rarefaction (depression) waves.

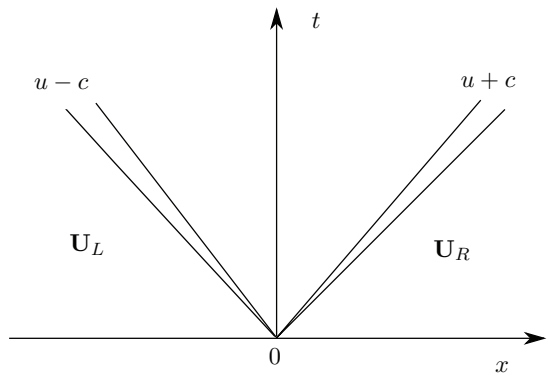

Figure 2.2. The wave structure for the Riemann problem.

A special case of the Riemann problem is when the velocities on the different sides of the discontinuity are initially zero but the water heights differ from each other. This is also known as the dam break problem and a sketch of the solution is illustrated in Figure 2.3. As can be seen from the figure, on the left side of the dam a smooth rarefaction wave starts travelling to the direction of the negative x-axis and a shock wave is travelling to the direction of the positive x-axis. The figure also shows the wave structure of the dam break problem in the $x - t$ plane.

The wave structure of the solution of the Riemann problem depends on the initial values on both sides of the discontinuity. For the shallow water equations the wave structure in a case where there are no dry regions may consist of two rarefaction waves, two shock waves, left rarefaction and a right shock wave or a right rarefaction and a left shock wave. When either

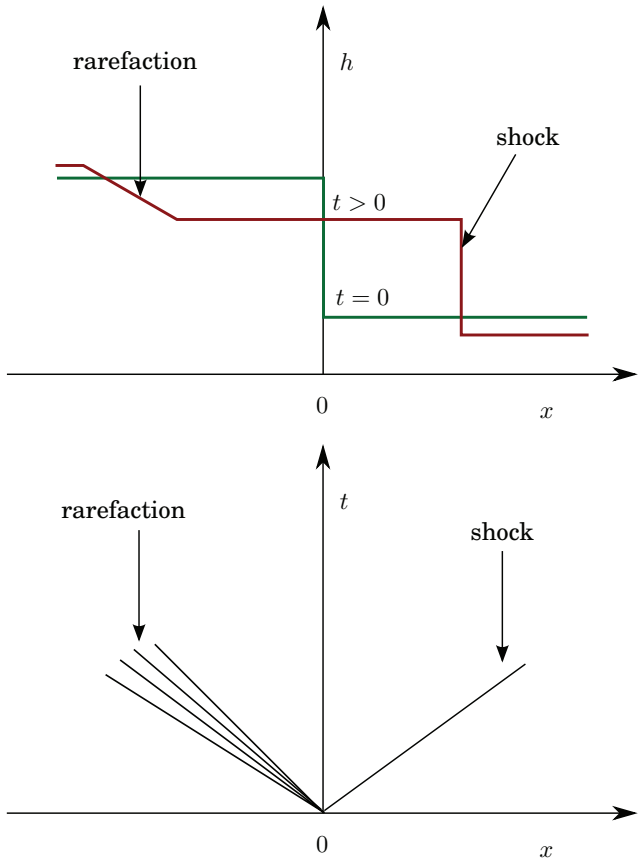

Figure 2.3. Illustration of the dam break problem. The first figure shows the evolution of the water height and the second figure shows the corresponding wave structure in the $x - t$ plane.

side of the initial values has a zero water depth the solution consists of a single rarefaction wave. The dry regions are discussed at the end of this section. The RCM is based on random sampling the exact Riemann solutions within each computational cell, therefore, it is necessary to consider all the possible wave structures of the solution.

2.3 The Riemann solution for shallow water equations

The Riemann solution at a cell interface can be derived by using the consistency of the Riemann invariants for the rarefaction waves and the Rankine-Hugoniot jump condition for the shock waves. In a wet bed case, the solution can be thought of consisting of a left, right and a middle (or star) region. The values within the star region are connected to the left and right regions with some functions f_L and f_R, respectively, as pre-

sented in Figure 2.4. Note that, although the two waves are drawn on different sides of the interface, both waves may very well propagate in the same direction. This is entirely determined by the charasteristic speeds at the interface.

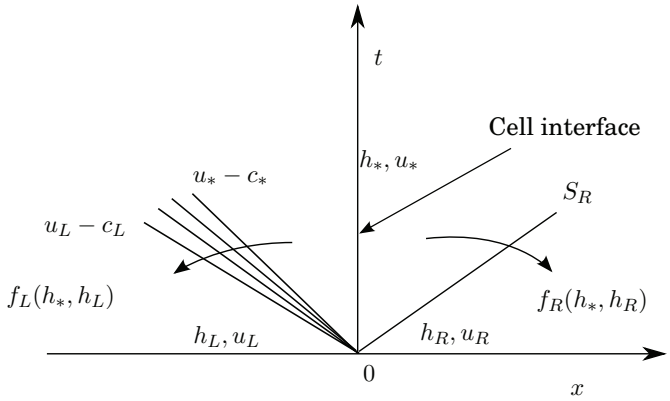

Figure 2.4. Example with a left rarefaction and a right shock wave.

Assuming a left rarefaction and a right shock wave, the function f_L connecting the star region to the left region can be found by using the primitive variables and the eigenvectors corresponding to the rarefaction

$$\begin{aligned}
\mathbf{W}_L &= \begin{bmatrix} w_{L,1} & w_{L,2} \end{bmatrix}^T = \begin{bmatrix} h_L & u_L \end{bmatrix}^T \\
\mathbf{W}_* &= \begin{bmatrix} w_{*,1} & w_{*,2} \end{bmatrix}^T = \begin{bmatrix} h_* & u_* \end{bmatrix}^T \\
\mathbf{v}_L &= \begin{bmatrix} v_{L,1} & v_{L,2} \end{bmatrix}^T = \begin{bmatrix} 1 & -c_L/h_L \end{bmatrix}^T \\
\mathbf{v}_* &= \begin{bmatrix} v_{*,1} & v_{*,2} \end{bmatrix}^T = \begin{bmatrix} 1 & -c_*/h_* \end{bmatrix}^T .
\end{aligned} \tag{2.22}$$

Using the method of charasteristics, the consistency of Riemann invariants

$$\frac{dw_{j,1}}{v_{j,1}} = \frac{dw_{j,2}}{v_{j,2}} \tag{2.23}$$

can be imposed across the rarefaction

$$\begin{aligned}
&\frac{dw_{*,1}}{v_{*,1}} = \frac{dw_{*,2}}{v_{*,2}} \Leftrightarrow \frac{dh_*}{1} = \frac{du_*}{(-c_*/h_*)} \\
&\Leftrightarrow du_* + \frac{c_*}{h_*} dh_* = 0.
\end{aligned} \tag{2.24}$$

Substituting $c_* = \sqrt{a_z h_*}$ and integrating Equation (2.24) leads to

$$\begin{aligned}
&\int du_* + \int \sqrt{a_z} h_*^{-1/2} dh_* = 0 \\
&\Leftrightarrow u_* + 2c_* = const
\end{aligned} \tag{2.25}$$

The constant of integration can be solved in a similar manner in terms of the known initial state $\mathbf{W}_L$. This leads to

$$u_* + 2c_* = u_L + 2c_L \tag{2.26}$$

and an expression for the star region velocity is found easily from the above equation

$$u_* = u_L - \underbrace{(2c_* - 2c_L)}_{f_L(h_*, h_L)}. \tag{2.27}$$

Since the celerity $c_* = \sqrt{a_z h_*}$ contains an unknown star region water height, another expression for u_* is required to solve the equation. This comes from applying the Rankine-Hugoniot jump condition to the right shock wave of Figure 2.4

$$\mathbf{F}(\mathbf{U}_R) - \mathbf{F}(\mathbf{U}_*) = S_R(\mathbf{U}_R - \mathbf{U}_*) \tag{2.28}$$

This results in two equations

$$\begin{aligned} &h_R u_R - h_* u_* = S_R(h_R - h_*) \\ &(h_R u_R^2 + \frac{1}{2} a_z h_R^2) - (h_* u_*^2 + \frac{1}{2} a_z h_*^2) = S_R(h_R u_R - h_* u_*) \end{aligned} \tag{2.29}$$

by solving the shock speed S_R from the first equation and substituting it to the second one, another expression for the star region velocity u_* can be obtained after tedious algebra [10]

$$u_* = u_R + \underbrace{(h_* - h_R)\sqrt{\frac{1}{2} a_z \left(\frac{(h_* + h_R)}{(h_* h_R)} \right)}}_{f_R(h_*, h_R)}. \tag{2.30}$$

The speed of the shock S_R, on the other hand, can be written as

$$S_R = u_R + c_R \sqrt{\frac{(h_* + h_R) h_*}{(h_R)^2}}. \tag{2.31}$$

Combining Equations (2.27) and (2.30)

$$u_L - f_L(h_*, h_L) = u_R + f_R(h_*, h_R), \tag{2.32}$$

the water height in the star region h_* can be numerically solved as the root of equation

$$\underbrace{(u_R - u_L) + f_R(h_*, h_R) + f_L(h_*, h_L)}_{f(h_*)} = 0. \tag{2.33}$$

In this work the root is found using the Newton-Raphson method alongside the bisection method to ensure that the iteration does not blow up when the derivative $f' = f'_L + f'_R$ is steep.

Although at this point, a certain wave structure for the Riemann solution at the interface has been assumed, the procedure described before can be expanded to other wave structures as well. The derivation of the connecting functions is identical. For example, in the case of right rarefaction wave and a left shock wave the functions of Equation (2.33) would be

$$\begin{aligned} f_L(h_*, h_L) &= (h_* - h_L)\sqrt{\frac{1}{2}a_z\left(\frac{(h_* + h_L)}{(h_* h_L)}\right)} \\ f_R(h_*, h_R) &= (2c_* - 2c_R) \end{aligned} \tag{2.34}$$

and for two rarefaction waves

$$\begin{aligned} f_L(h_*, h_L) &= (2c_* - 2c_L) \\ f_R(h_*, h_R) &= (2c_* - 2c_R) \end{aligned} \tag{2.35}$$

or two shock waves

$$\begin{aligned} f_L(h_*, h_L) &= (h_* - h_L)\sqrt{\frac{1}{2}a_z\left(\frac{(h_* + h_L)}{(h_* h_L)}\right)} \\ f_R(h_*, h_R) &= (h_* - h_R)\sqrt{\frac{1}{2}a_z\left(\frac{(h_* + h_R)}{(h_* h_R)}\right)}. \end{aligned} \tag{2.36}$$

The conditions which determine whether a wave is a rarefaction or a shock wave are [9]

$$\begin{aligned} h_* > h_{L/R} &\rightarrow \text{The wave is a shock} \\ h_* \leq h_{L/R} &\rightarrow \text{The wave is a rarefaction} \end{aligned} \tag{2.37}$$

The initial wave structure at the beginning of the iteration is assumed to be two rarefaction waves in the case when $h_*^0 < \min(h_L, h_R)$ and two shock waves when $h_*^0 > \min(h_L, h_R)$. However, since the bisection method ensures that the iteration stays in bounds, the choice of the initial guess is not that critical. It should be noted that the wave structure and thus the functions f_L and f_R and their derivatives may very well change during the iteration. Therefore, the conditions (2.37) have to be tested during each iteration of the root-finding algorithm and the functions f_L and f_R and the derivatives have to be calculated accordingly.

After the star region water height is found, the velocity in the star region can be found using a mean value

$$u_* = \frac{1}{2}(u_L + u_R) + \frac{1}{2}(f_R(h_*, h_R) - f_L(h_*, h_L)). \tag{2.38}$$

Although, negative water heights are obviously unphysical, dry regions in the spatial domain may very well exists and their treatment requires some extra attention. As can be seen from Equations (2.36), functions f_R

and f_L connecting the star region to the left and right states in the case of a shock wave are not defined when the water height at some part is zero. As an example, let us consider the previously presented dam break case when the water height at the right side of the dam is zero as in Figure 2.5.

If we assume that the occurring wave is a shock, we can again apply the Rankine-Hugoniot condition

$$\begin{aligned} &h_L u_L - h_R u_R = S_L(h_L - h_R) \\ &(h_L u_L^2 + \frac{1}{2} a_z h_L^2) - (h_R u_R^2 + \frac{1}{2} a_z h_R^2) = S_L(h_L u_L - h_R u_R) \end{aligned} \tag{2.39}$$

for $h_R = 0$ the equations are

$$\begin{aligned} &h_L u_L = S_L(h_L) \Leftrightarrow S_L = u_L \\ &(h_L u_L^2 + \frac{1}{2} a_z h_L^2) = S_L(h_L u_L) \end{aligned} \tag{2.40}$$

substituting $S_L = u_L$ to the second equation

$$\begin{aligned} &(h_L u_L^2 + \frac{1}{2} a_z h_L^2) = (h_L u_L^2) \\ &\Leftrightarrow h_L = 0, \end{aligned} \tag{2.41}$$

which clearly violates the assumption $h_L > 0$ of the initial state. A similar procedure can be applied to the case of the dry region being on the left side of the dam, indicating that a shock wave can not be adjacent to a dry region. Furthermore, a more important observation can be made from the above example, viz., the wave structure of the solution changes when there are dry regions to be considered.

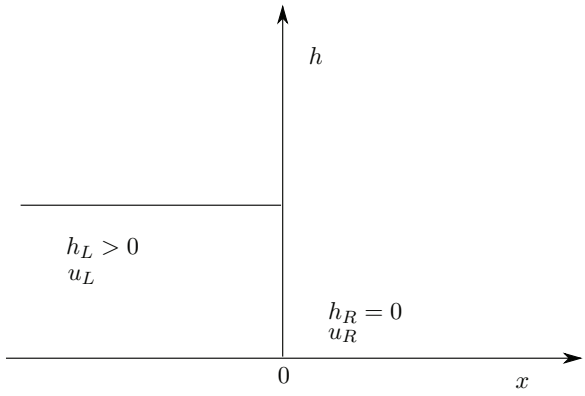

Figure 2.5. The dam break with zero water height.

Thus the Riemann solutions derived at this point are only useful for cases where there are no dry regions. To determine whether the Riemann

solutions for the wet bed cases can be used, a depth-positivity condition is tested before the solution at the cell interface

$$\begin{aligned} & f(h_* = 0) > 0 \\ \Leftrightarrow\ & (u_R - u_L) - 2(c_R + c_L) > 0. \end{aligned} \tag{2.42}$$

If Equation (2.42) is not fulfilled, a different wave structure occurs and the possible structures are presented next.

As shown before, a shock wave can not be adjacent to a dry state. Thus the wave structure of the Riemann solution for the case in Figure 2.5 is a single left rarefaction wave corresponding to eigenvalue $\lambda = u - c$. The wave stucture of the solution in $x-t$ plane is illustrated in Figure 2.6. The right bound for the rarefaction can be found, again, using the consistency of Riemann invariants across the rarefaction

$$u_R + 2c_R = u_L + 2c_L, \tag{2.43}$$

where the celerity $c_R = \sqrt{a_z h_R} = 0$ since $h_R = 0$. The speed of the discontinuity and the right bound for the rarefaction is $S_{DL} = u_L + 2c_L$.

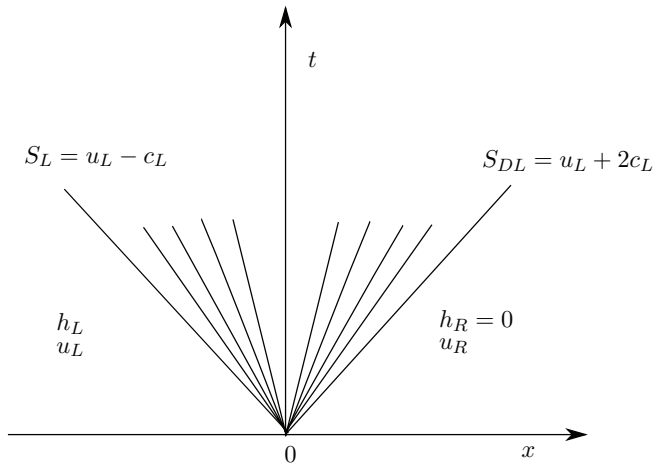

Figure 2.6. The wave structure of the dry right state case.

If the dry region is on the left, the solution is also a single rarefaction but it is now associated with eigenvalue $\lambda = u + c$. The left and right bounds for the rarefaction are found in almost identical manner as $S_{DR} = u_R - 2c_R$ and $S_R = u_R + c_R$ respectively.

There is also a special case when the dry region appears between the left and right regions. This may occur with a suitable combination of u_R and u_L, which do not satisfy the depth positivity condition, although both the left and right states have positive water height. In this case, the solution

consists of two rarefaction waves associated with eigenvalues $\lambda = u \pm c$ (see Figure 2.7).

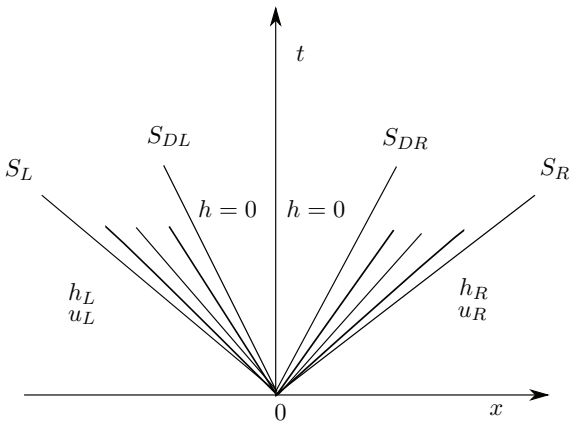

Figure 2.7. The wave structure of the dry middle state.

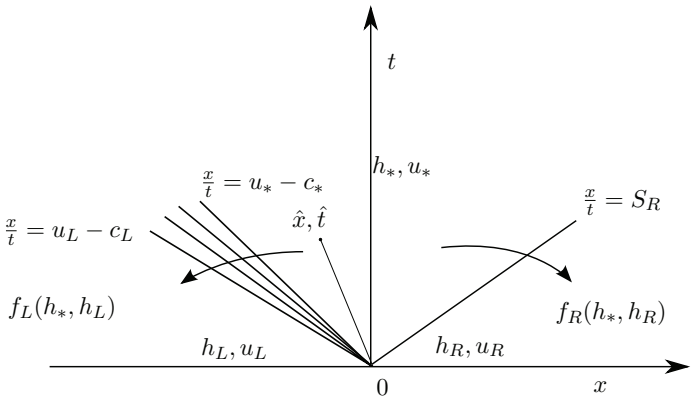

Figure 2.8. Sampling the Riemann solution at a cell interface.

At this point a piecewise solution for the Riemann problem at a cell interface has been constructed. To summarize, a sample point $\hat{x}, \hat{t}$ in the $x-t$ plane with a charasteristic speed $\hat{x}/\hat{t}$ can be considered. The solution at time $\hat{t}$ for the wave structure of Figure 2.8 before the left rarefaction is defined as

$$\left.\begin{array}{l} u = u_L \\ c = c_L \end{array}\right\} \text{ if } \frac{\hat{x}}{\hat{t}} < (u_L - c_L). \tag{2.44}$$

Inside the rarefaction the solution can be found by using the generalized Riemann invariants and the speed of the charasteristic

$$\begin{aligned} u + 2c &= u_L + 2c_L \\ u - c &= \frac{\hat{x}}{\hat{t}} \end{aligned} \tag{2.45}$$

resulting in

$$\left.\begin{aligned} u &= \frac{1}{3}\left(u_L + 2c_L + \frac{2\hat{x}}{\hat{t}}\right) \\ c &= \frac{1}{3}\left(u_L + 2c_L - \frac{\hat{x}}{\hat{t}}\right) \end{aligned}\right\} \text{ if } (u_L - c_L) \leq \frac{\hat{x}}{\hat{t}} < (u_* - c_*) \tag{2.46}$$

for the region inside the rarefaction wave.

The star region is bounded by the charasteristic speed of the tail $u_* - c_*$ of the rarefaction and the speed of the shock wave S_R (see Equation (2.31)). The solution inside the star region is

$$\left.\begin{aligned} u &= u_* \\ c &= c_* \end{aligned}\right\} \text{ if } (u_* - c_*) \leq \frac{\hat{x}}{\hat{t}} \leq S_R. \tag{2.47}$$

Finally, in the region right of the shock wave the solution is

$$\left.\begin{aligned} u &= u_R \\ c &= c_R \end{aligned}\right\} \text{ if } \frac{\hat{x}}{\hat{t}} > S_R. \tag{2.48}$$

In practice, however, the point $\hat{x}$ is chosen within each cell and $\hat{t} = \Delta t$. The Riemann problem is solved only at the cell interface which is closest to the chosen point (see Figure 2.9)

$$\mathbf{W}_i^{n+1} = \begin{cases} \mathbf{W}_{i-1/2}(\theta^n \Delta x/\Delta t) & \text{if } 0 \leq \theta \leq 1/2 \\ \mathbf{W}_{i+1/2}((\theta^n - 1)\Delta x/\Delta t) & \text{if } 1/2 < \theta \leq 1 \end{cases} \tag{2.49}$$

where $\mathbf{W}_{i\pm1/2}^n$ denotes the Riemann problem solution at the cell interface at time level n and $\theta^n \in [0,1]$ is a pseudorandomly chosen variable. The justification of randomly choosing a single point is discussed to some extent in the following sections. The initial (left and right) values for the Riemann problem are taken from the neighbouring nodal values, again, depending on the value of θ and the cell interface which the Riemann problem is solved at.

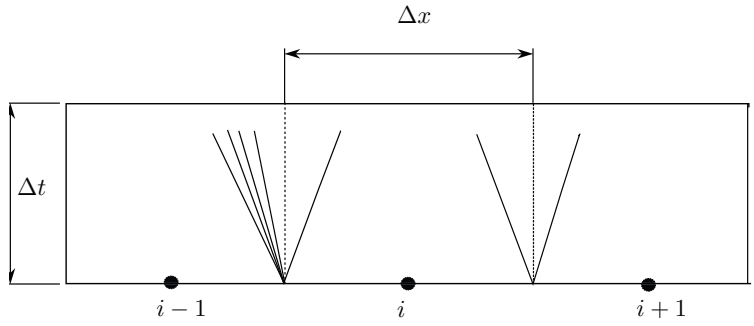

Figure 2.9. The solution in cell i.

3. Random choice method

3.1 Outline of Glimm's proof

The RCM was presented by James Glimm in his celebrated paper [4], where he not only showed that weak solutions for the Riemann problem exist but also developed a method for solving the problem when the oscillation of the initial values are (and remain) sufficiently small. The outline of Glimm's method and proof is presented in this chapter.

Glimm studied the weak solutions of initial value problem

$$\begin{aligned} u_t + f(u)_x &= 0 \\ u(x,0) &= u_0(x), \end{aligned} \tag{3.1}$$

where u_0 denotes the initial values and $f(u)$ and u are m-vectors. The system is assumed to be smooth and strictly hyperbolic, meaning that the Jacobian $\frac{\partial f(u)}{\partial u}$ has m real eigenvalues $\lambda(u)_1 < \lambda(u)_2 < \lambda(u)_m$. A function $u(x,t)$ is a weak solution of Equation (3.1) if it satisfies

$$\int_0^\infty \int_{-\infty}^\infty \left[u\frac{\partial \varphi}{\partial t} + f(u)\frac{\partial \varphi}{\partial x} \right] dxdt + \int_{-\infty}^\infty u_0 \varphi(x,0)\, dx = 0 \tag{3.2}$$

for any smooth function $\varphi(x,t)$ in $t \geq 0$.

In Glimm's method, the exact solution is obtained as $\Delta x \to 0$ of approximate solution $u_{\Delta x}$. First assuming at time $n\Delta t$ that the approximate solution is constant on spatial intervals of Δx (discretized cells)

$$u_{\Delta x}(x, n\Delta t) = u^n \quad \text{for} \quad (i-1/2)\Delta x < x < (i+1/2)\Delta x, \tag{3.3}$$

where $i = 0, \pm 1, \pm 2 \ldots$ At time level $n+1$, we wish to compute a new solution with the same property

$$u_{\Delta x}(x, (n+1)\Delta t) = u_i^{n+1} \quad \text{for} \quad (i-1/2)\Delta x < x < (i+1/2)\Delta x. \tag{3.4}$$

Glimm suggested that a sequence of prechosen random numbers $\{\theta_i^n\}, \theta_n^i \in (0,1)$ could be used to construct the solution at the new time level. Thus the exact solution of the Riemann problems are denoted as $u_e^n(x,t)$ for $n\Delta t < t < (n+1)\Delta t$ with initial values from the previous time level. The solution at the new time level is then

$$u_i^{n+1} = u_e^n((i - 1/2 + \theta_i^{n+1})\Delta x, (n+1)\Delta t). \tag{3.5}$$

Glimm proved that these solutions $u_e^n(x,t)$ exist for all t by showing that the oscillation of the initial values remains small for all $n = 1, 2...$ and that the waves occurring at $x = i \pm 1/2$ do not overlap. That is, some constant independent of $\Delta x, \Delta t$ and the random sequence can always be chosen, which satisfies

$$T.V.(u_{\Delta x}(x,t,\theta_i^n)) \leq const.(T.V.(u_0)), \tag{3.6}$$

where $T.V.$ denotes the total variation over $x \in (-\infty, \infty)$

$$T.V.(u) = \int_{-\infty}^{\infty} \left| \frac{\partial u}{\partial x} \right| dx. \tag{3.7}$$

Since the approximate solution $u_{\Delta x}$ obtained using the Glimm's method is not exact in all $x \in (-\infty, \infty)$, Equation (3.2) gets the form

$$\begin{aligned} \int_0^{\infty} \int_{-\infty}^{\infty} \left[u_{\Delta x} \frac{\partial \varphi}{\partial t} + f(u_{\Delta x}) \frac{\partial \varphi}{\partial x} \right] dx dt + \int_{-\infty}^{\infty} u_{\Delta x}(x,0)\varphi(x,0)\, dx \\ = \sum_{n=0}^{\infty} E(\Delta x, \varphi, \theta_i^n), \end{aligned} \tag{3.8}$$

where $E(\Delta x, \varphi, \theta_i^n)$ is the error defined as

$$E(\Delta x, \varphi, \theta_i^n) = \int_{-\infty}^{\infty} \left(u_{\Delta x}(x, n\Delta t + 0) - u_{\Delta x}(x, n\Delta t - 0) \right) \varphi(x, \Delta t)\, dx. \tag{3.9}$$

Using Helly's selection principle [11], Glimm showed that

$$\| E(\Delta x, \varphi, \theta_i^n) \| \to 0 \text{ as } \Delta x \to 0 \tag{3.10}$$

for almost any sequence $\{\theta_i^n\}$ and thus the approximate solution converges to the weak solution of Equation (3.1). For more details on the proof the reader is referred to [4, 11, 12].

The limits of the spatial and temporal increments can be deduced from the fact that the waves occurring at $x = i \pm 1/2$ should not intersect (see Figure 3.1)

$$\frac{\Delta t \lambda_i}{\Delta x} < \frac{1}{2}. \tag{3.11}$$

In practice, however, the time step is adjusted in a way that Equation (3.11) is satisfied

$$\begin{aligned} \Delta t &= C\frac{\Delta x}{\lambda^n_{max}} \\ \lambda^n_{max} &= \max_i(|u^n_i| + c^n_i), \end{aligned} \tag{3.12}$$

where $0 < C < 1/2$ is some suitable value. In this work $C = 0.45$ is used as suggested in [9].

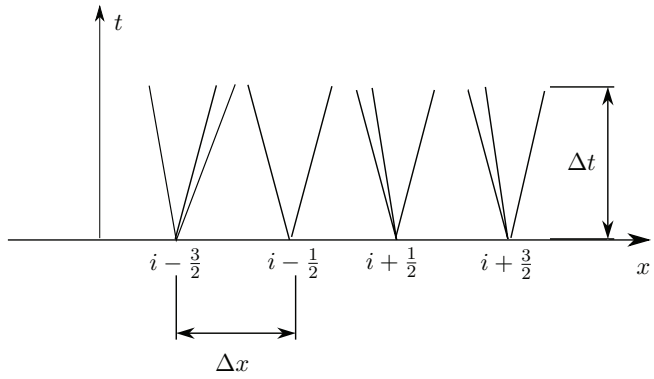

Figure 3.1. Waves occuring at the cell interfaces.

It should be noted that the rate of the convergence depends on the chosen sequence $\{\theta^i_n\}$. Originally, Glimm proposed choosing a different random value for all i and n but later Chorin [5] proposed using the same random number for all i at each time level to maximize the rate of convergence and to avoid spurious constant states occurring from waves propagating to both left and right.

Additionally, in Glimm's original paper [4], it is stated that the method converges using *almost* any random sequence. However, Liu [13] showed that the method converges using *any* equidistributed sequence making the method deterministic rather than stochastic.

3.2 Choice of the random sequence

The choice of the optimal random sequence was studied quite thoroughly by Colella in [14]. Since the rate of convergence and the accuracy of the RCM depends on the rate at which the random sequence approaches a uniform distribution in the sampling range, Colella suggested the use of the van der Corput pseudorandom sequence in the sampling procedure and it is also applied in this work.

The van der Corput sequence is defiend as [15]

$$\begin{aligned} \theta^n &= \sum_{j=0}^{m} A_j k_1^{-(j+1)} \\ A_j &= k_2 a_j \mod (k_1) \\ n &= \sum_{j=0}^{m} a_j k_1^j, \end{aligned} \tag{3.13}$$

where k_1 and k_2 are relatively prime integers and $k_1 > k_2$. To apply the sequence, one first solves a_j from the last equation of (3.13) and then the corresponding A_j from the middle equation. Finally, the value of θ^n can be solved from the first equation.

As an example, the pseudo-random number $\theta^{n=100}$ with $(k_1, k_2) = (5, 3)$ can be calculated as follows

$$\begin{aligned} & n = \sum_{j=0}^{m} a_j k_1^j \;\Leftrightarrow\; 100 = \underbrace{0}_{a_0} \times 5^0 + \underbrace{0}_{a_1} \times 5^1 + \underbrace{4}_{a_2} \times 5^2 \\ & A_j = k_2 a_j \mod (k_1) \Leftrightarrow A_0 = 0, \;\; A_1 = 0, \;\; A_2 = 2 \\ & \theta^{100} = \sum_{j=0}^{2} A_j k_1^{-(j+1)} = 0 \times 5^{-1} + 0 \times 5^{-2} + 2 \times 5^{-3} = 0.016. \end{aligned} \tag{3.14}$$

The values a_j can be easily calculated by noting that the last equation in (3.13) is exactly the base-k_1 expression of n. If $k_1 = 2$, the binary expression of n is obtained and if $k_1 = 5$, as in the example above, the quinary expression of n is obtained. An algorithm for the pseudorandom number generation is presented below.

while (test > 1) **do**
  test $= n/k_1^j$
  $a_j =$ test $\mod (k_1)$
  $A_j = k_2 a_j \mod (k_1)$
  $\theta = \theta + A_j k_1^{-(j+1)}$
  $j = j + 1$
end while

The optimal choice of values k_1 and k_2 is discussed in [14] and [15]. Here the values $(k_1, k_2) = (5, 3)$ are used as suggested in [15].

3.3 Source terms and boundary conditions

The source terms in the equations are handled by applying the operator splitting technique. The technique, in the framework of RCM, was first

applied by Chorin in [5] to extend the method to multidimensional problems and by Sod in [16] for source terms of a cylindrical shock. In [6] Dillingham applied the RCM with operator splitting to couple the motion of a shallow water on a ship deck to the motion. The operator splitting is applied to shallow water equations by first removing the inhomogeneous term on the RHS of the momentum equation in (2.13). In operational splitting, the shallow water equations are first solved without the source term

$$\begin{aligned} &\frac{\partial h}{\partial t} + \frac{\partial (hu)}{\partial x} = 0 \\ &\frac{\partial u}{\partial t} + u\frac{\partial u}{\partial x} + a_z \frac{\partial h}{\partial x} = 0 \end{aligned} \tag{3.15}$$

using the RCM described in the previous sections. When the RCM solution is available, the source terms are taken into account by solving

$$\frac{\partial u^{rcm}}{\partial t} = f_x. \tag{3.16}$$

In this work, Equation (3.16) is solved using simple Euler time integration

$$\frac{u^{n+1} - u^{rcm}}{\Delta t} = f_x. \tag{3.17}$$

Since the RCM is first order accurate, there is no reason to use higher order approximations in the splitting phase.

In the numerical experiments of this work, the motion of the domain is handled through the source terms. If the motion of the domain is restricted to the X, Z-plane as in Figure 2.1 and translation is neglected, the body forces affecting on a fluid particle are

$$\begin{aligned} f_x &= -2\Omega h \frac{\partial u}{\partial x} - g\sin\phi + \dot{\Omega}(z-h) + \Omega^2 x \\ a_z &= g\cos\phi + 2\Omega u + \dot{\Omega} x - \Omega^2 h. \end{aligned} \tag{3.18}$$

Here the velocities in Equation (3.18) are taken explicitly from the previous time level and the spatial derivative in f_x is approximated using the central difference

$$\frac{\partial u}{\partial x}|_i \approx \frac{u_{i+1} - u_{i-1}}{2\Delta x}. \tag{3.19}$$

Additionally, the z-coordinate appearing in f_x is set to average water height $z_i = h_i/2$.

The boundary conditions at the left and right ends of the domain are applied using imaginary (ghost) nodes just outside the domain. The values of the ghost nodes are assigned in a way that assures the solution of

the corresponding domain nodes to get correct values when the Riemann problems are solved. In all numerical experiments of this study, the left and right ends of the domain are treated as solid unmoving walls. The ghost cell values, which assure the correct solution at the domain ends are

$$\begin{aligned} &h_0 = h_1, \;\; u_0 = -u_1 \\ &h_{imax+1} = h_{imax}, \;\; u_{imax+1} = -u_{imax}, \end{aligned} \tag{3.20}$$

where subscripts 0 and $imax + 1$ denote the ghost nodes at the left and right ends, respectively.

4. Numerical experiments

4.1 The dam break problem

Already in the derivation of the shallow water equations, several simplifying assumptions about the flow physics were made. Therefore, to evaluate the applicability of the method it is necessary to compare the results both to experimental as well as analytical data to ensure that the cumulative error made in the assumptions and approximations of the numerical scheme is reasonable.

The first numerical experiment is the classic dam break problem already described to some extent in Chapter 2. In this section, the results calculated with the RCM are compared to both the analytical solution as well as to experimental results by Lobovsky et al. [17].

In the analytical case, the domain length is $x \in [-5, 5]$ m with an initial water height $H = 0.3$ m at the right half of the domain ($x \in [0, 5]$ m). The left side of the domain has an initial water depth of zero and the initial velocity is zero in the whole domain. In the RCM results, the domain is discretized into 100 equally spaced nodes and the time step is altered according to Equation (3.12) to ensure that the waves of the Riemann problem solutions do not overlap.

The analytic solution corresponds to the dry right state Riemann solution and it is given as

$$\mathbf{W}_{an} = \begin{cases} \mathbf{W}_L & \text{if } x/t \leq u_R - 2c_R \\ \mathbf{W}_{rare} & \text{if } u_R - 2c_R < x/t \leq u_R + c_R \\ \mathbf{W}_R & \text{if } x/t > u_R + c_R, \end{cases} \tag{4.1}$$

where the rarefaction wave solution is

$$\mathbf{W}_{rare} = \begin{cases} c = (-u_R + 2c_R + x/t)/3 \\ u = (u_R - 2c_R + 2x/t)/3. \end{cases} \tag{4.2}$$

The water height and velocity at time $t = 1$ s are presented in Figure 4.1. As can be seen from the figure, the RCM results are almost identical to the analytic solution. Furthermore, the discontinuities in the solution are captured very well and the dry region in the domain remains dry. For many other schemes the dry regions in the domain can be extremely problematic.

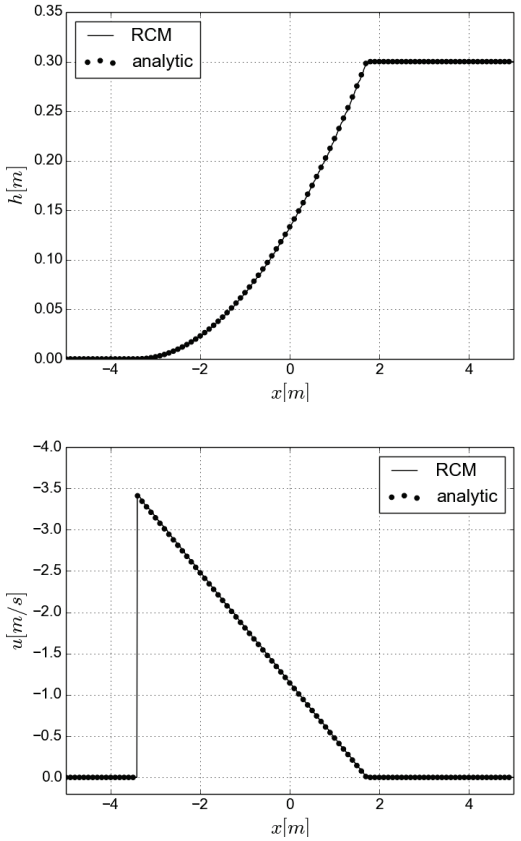

Figure 4.1. The RCM results compared to the analytical solution of the dam break problem at $t = 1$ s.

A sketch of the geometry in the Lobovsky et al. measurement is presented in Figure 4.2. The grey region in the figure is the initial water in the tank and the locations H1...H4 denote the locations where the water level was measured. The depth of the tank into the paper (160 mm) in the experiment was chosen so that wall effects could be considered as not

affecting the main flow dynamics and the top of the tank was open. More details on the experimental setup and equipment can be found in [17].

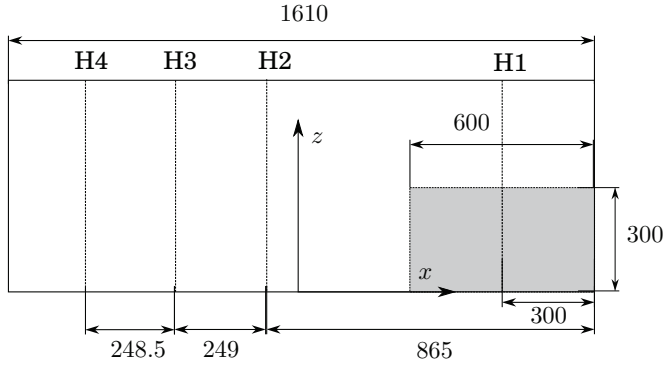

Figure 4.2. A sketch of the Lobovsky et al. experiment. The dimensions in the figure are in millimeters.

The results of the RCM simulation are presented and compared to measurements in Figure 4.3. The water heights are scaled by the initial water height $H = 300$ mm and the time on the x-axis by $(g/H)^{1/2}$. The primary wave in the figure denotes the arrival of the first wave front to the measurement location and the secondary wave the arrival of the wave front which has reflected from the left wall of the tank.

As can be seen from the figure, the calculated results are quite close to the measurements and the overall shape of the curves are very similar in the experimental and RCM data. However, the primary waves seem to arrive earlier in the RCM results at all measurement locations and the secondary waves arrive later with the exception of H4 measurement location. Since the primary waves arrive earlier in the RCM results to all measurement locations with initial water depth of zero, it would be intuitive that the secondary wave reflected from the left wall would also arrive earlier. But this is only the case at the leftmost measurement location (H4). At locations H3-H1 the RCM results show that the wave front arrives after the measured wave front. This is most likely caused by the combination of wave breaking and turbulence effects which are not accounted for in the one-dimensional RCM results. However, the height of the wave front is quite well captured and the overall results are satisfactory.

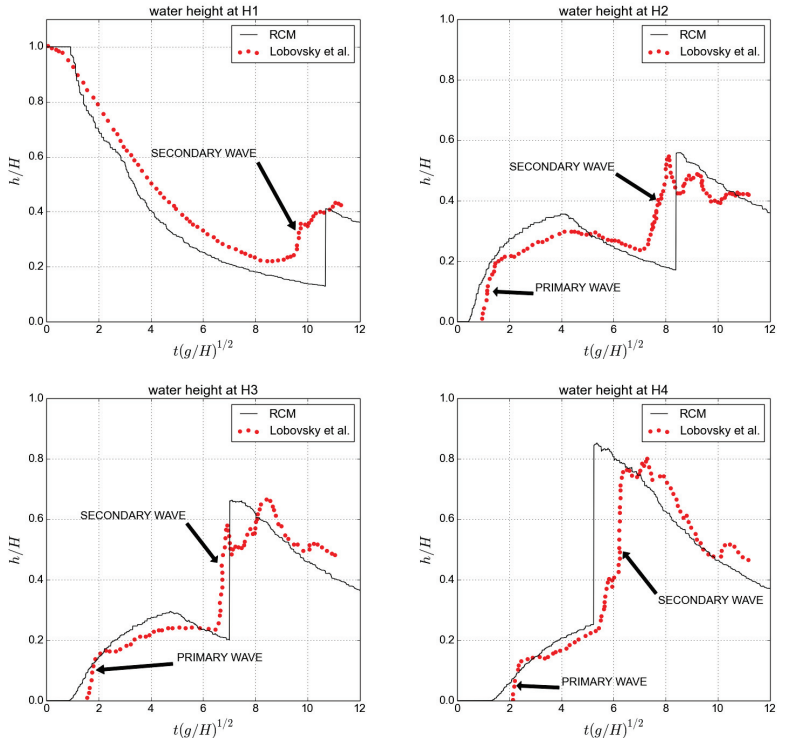

Figure 4.3. The simulated water heights at the measurement locations as a function of time compared to experimental data.

4.2 Periodic roll motion

The second numerical experiment is based on the sloshing experiment by Delorme et al. [18]. In the experiment, a rectangular tank with dimensions $0.9 \times 0.05 \times 0.58$ m^3 in the x-, y- and z-directions, respectively, was excited with a sinusoidal rotating motion around the y-axis. The coordinate system in the setup is the same as in Figure 2.1. The amplitude of the rotational motion was $\phi_{max} = 4°$ and results were measured with three different oscillation periods $T = 2.112$ s, 1.920 s, 1.728 s. The initial free-surface was horizontal and the initial depth in the tank was $H = 0.093$ m. In the RCM calculations the spatial spacing was set to $\Delta x = 0.005$ m resulting in 180 equally spaced nodes.

The dimensionless pressure as a function of dimensionless time on the left side of the tank is presented in Figure 4.4. In the experimental data the pressure sensor was placed at the initial water height, therefore, the pressure of the corresponding RCM data is given as $p = \rho a_z(h - H)$. Furthermore, a low-pass filter was used in the measurements in order to reg-

ister the pressure values without additional noise. As can be seen from the figure, the RCM results follow qualitatively the experimental ones with both showing a periodic behavior. However, the maximum values of the pressure are underestimated in the RCM results and there seems to be an increasing phase error when the period of the tank excitation is shorter. With $T = 1.728$ s the phase lag in the RCM results is already quite severe and the maximum values are not even close to the experimental ones with the exception of the first impact.

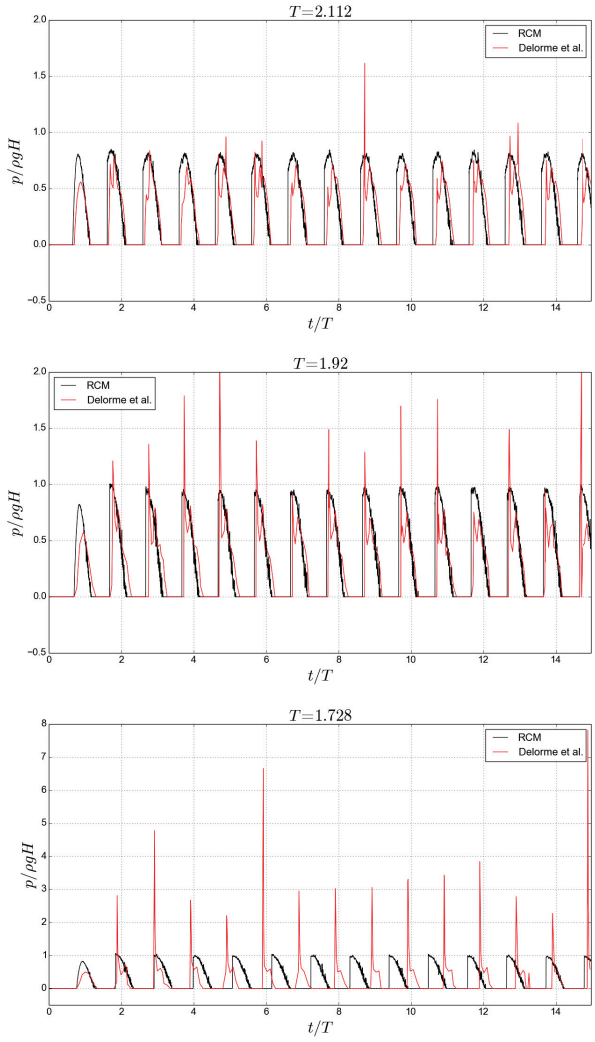

Figure 4.4. The dimensionless pressures on the left side of the tank as a function of time.

Figure 4.5 shows a closer view of the second impact on the wall. The experimental results show three local maximums in the impact curves, from which the first one is caused by the impact of the front of the wave

and the second and third ones from the remaining of the wave arriving to the wall. When $T = 1.728$ s the front wave arrives to the wall when the tank is already moving to the opposite direction causing a higher first maximum than in the other two cases [18]. As the RCM is not capable of capturing the physical structure of the wave correctly, the impact curves show only the arrival of the wave front and with the longest period ($T = 2.112$ s) the change of direction in the tank motion.

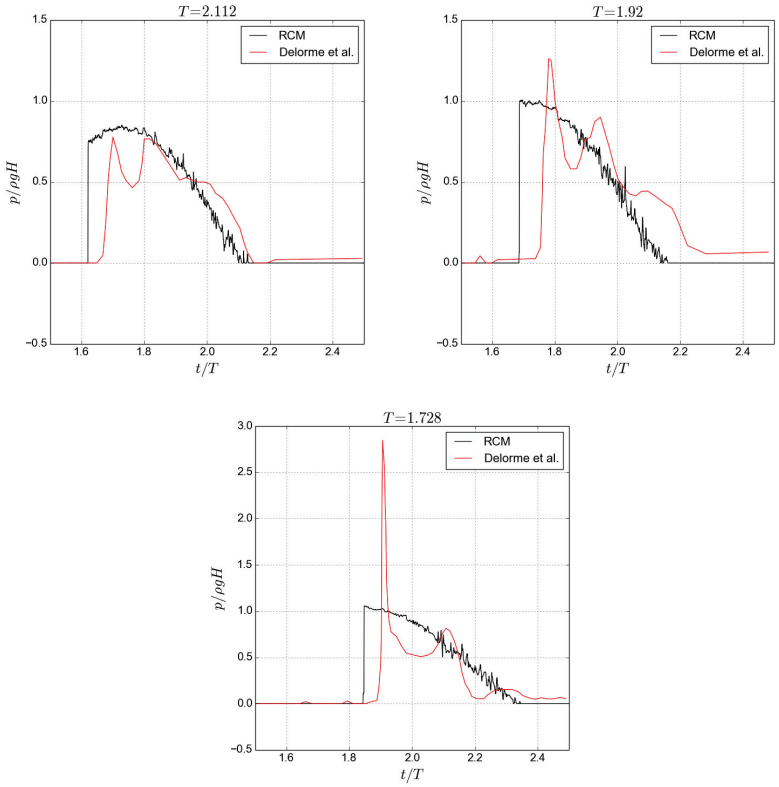

Figure 4.5. A closer view of the second impacts on the left wall.

The water levels at different time instances in the $T = 1.92$ s case are presented in Figure 4.6. As can be seen from the figure, at the first time instance (F1) the wave in the RCM results has already reached the left wall whereas in the experimental results the wave front is just about to hit the wall. The phase lead in the RCM results is evident at all time instances. Furthermore, the RCM wave structure is much sharper than the experimental one as the experimental wave breaks during the measurement at approximately time instance F4.

Another quite crucial flaw of the RCM method is that due to (pseudo) randomness of the method, the RCM conserves mass only on the time

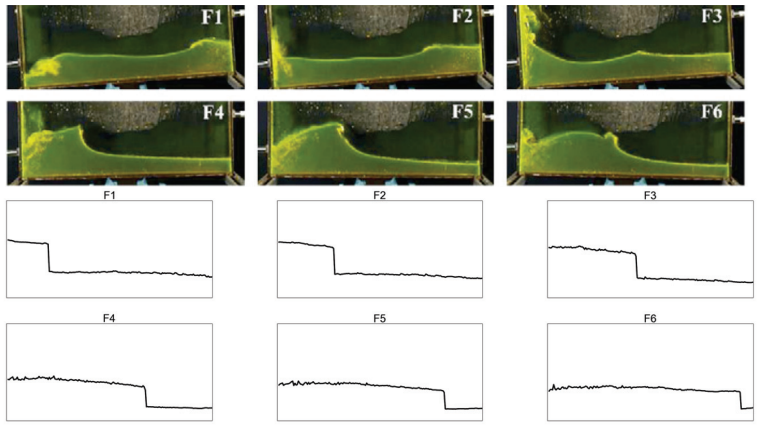

Figure 4.6. Water levels at $t = 16.85, 16.93, 17.11, 17.34, 17.45, 17.55$ corresponding to images F1-F6 respectively. In both the experimental [18] and the RCM results the length scale is approximately the same with the y-coordinate ranging from zero to a half height of the tank. The phase lead in the RCM results is evident at all time instances.

avarage. This is illustrated in Figure 4.7, where the amount of water in the tank is presented as a function of time. With the longest period of excitation mass is conserved reasonably well but with the two other periods oscillations are quite substantial. The capability of RCM conserving mass depends quite heavily on the frequency of the excitation and the time step used (value C in Equation (3.12)). With lower frequencies of excitation mass is conserved better. Mass conservation issues in the framework of RCM have been reported in other works as well, see for example [6, 19] and the comments by Armenio in [20].

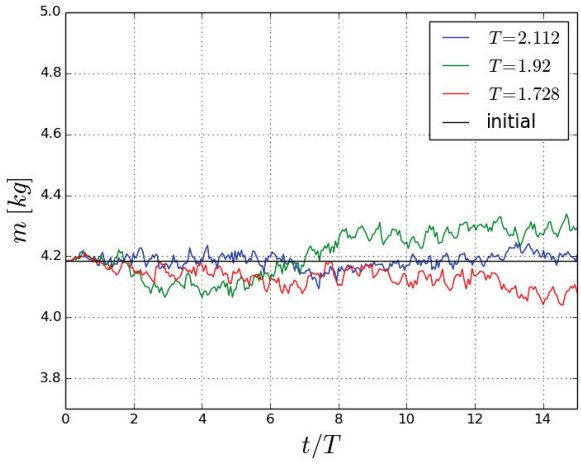

Figure 4.7. The mass of water in the tank as a function of time in the RCM simulations.

5. Discussion

In this work the RCM was presented and applied to the one-dimensional shallow water equations along with operational splitting to take into account the external forces caused by the motion of the domain. For the dam break problem, the results presented here were quite good but for the shallow water sloshing case some error occurred. The error grew when the frequency of the roll excitation was increased and the fluid motion was physically more complex due to breaking waves and high dissipation caused by turbulence. Furthermore, domain motion and additional source terms in the equations caused higher variation in the conservation of mass, again, increasing as the excitation frequency was increased. Similar behavior of the RCM has also been reported by others.

It was shown that the RCM is capable of sharply capturing discontinuities and dry regions in the domain with relatively coarse spatial and temporal discretization. This is not the case for many other numerical schemes and especially the dry regions in the domain are very problematic. A good comparison of different numerical schemes for the shallow water equations is given in [9]. The RCM behaved well when the motion of the domain and dry regions occurred simultaneously, however, the results of such a case are not presented here.

Although the higher frequencies of domain excitation caused some issues, the RCM behaves well on lower frequencies even if the motion amplitude (maximum rotation angle) is large. This indicates that the method could possibly be utilized in, for example, calculating the motion of floodwater excited by a vessel in waves since the frequency of the vessel motion is typically quite low. However, this requires further study and testing since the motion of the vessel is usually three-dimensional with translation and rotation in the direction and around all coordinate axes.

The RCM has been utilized for two-dimensional shallow water equations

by Dillingham & Falzarano in [21] and by Santos & Soares in [22]. They utilized the operational splitting technique first to reduce the problem to two sets of one-dimensional Riemann problems and then again when coupling the domain motion and the fluid motion. In both papers, relatively good results were obtained, although, in the paper by Dillingham & Falzarano comparison to experimental results was quite minimal. The conservation of mass was not commented on either of the papers.

However, in [14] Colella used the RCM and operational splitting technique to solve the two-dimensional Euler equations but stated that the actual justification of the splitting technique is unknown and likely to be different from the usual truncation error analysis of difference-type schemes. The results he obtained for the two-dimensional problem were poor. Instead he suggested the use of a hybrid Godunov-Glimm (RCM) scheme, in which the conservative Godunov scheme is applied to the parts where strong pressure jumps occur and the RCM everywhere else. The Godunov scheme is essentially an integral average of the exact Riemann solution in a cell and it results in an unnecessary smoothing (diffusion) of the wave structure but ensures that the error near strong pressure jumps remains at an order of $O(1)$ after sweeps in both spatial dimensions. Similar hybrid schemes have been introduced by others as well (see for example [23]).

To summarize, if the motion of the domain is restricted to X, Z-plane and the frequency of the motion is low the RCM can be utilized to solve the fluid motion. However, if the motion of the domain is three-dimensional some other approach may have to be used. The hybrid schemes will most likely work better but their behavior near the dry regions of the domain is not known. More study on the subject is needed.

Bibliography

[1] C. W. Hirt and B. D. Nichols, "Volume of fluid (vof) method for the dynamics of free boundaries," *Journal of computational physics*, vol. 39, no. 1, pp. 201–225, 1981.

[2] G. Liu, M. Liu, and S. Li, "Smoothed particle hydrodynamics—a meshfree method," *Computational Mechanics*, vol. 33, no. 6, pp. 491–491, 2004.

[3] P. L. Roe, "Approximate riemann solvers, parameter vectors, and difference schemes," *Journal of computational physics*, vol. 43, no. 2, pp. 357–372, 1981.

[4] J. Glimm, "Solutions in the large for nonlinear hyperbolic systems of equations," *Communications on Pure and Applied Mathematics*, vol. 18, no. 4, pp. 697–715, 1965.

[5] A. J. Chorin, "Random choice solution of hyperbolic systems," *Journal of Computational Physics*, vol. 22, no. 4, pp. 517–533, 1976.

[6] J. Dillingham, "Motion Studies of a Vessel with Water on Deck," *Marine Technology*, vol. 18, no. 1, pp. 38–55, 1981.

[7] G. Marshall and R. Méndez, "Computational aspects of the random choice method for shallow water equations," *Journal of Computational Physics*, vol. 39, no. 1, pp. 1–21, 1981.

[8] V. Armenio and M. La Rocca, "On the analysis of sloshing of water in rectangular containers: numerical study and experimental validation," *Ocean Engineering*, vol. 23, no. 8, pp. 705–739, 1996.

[9] E. F. Toro, *Shock-capturing methods for free-surface shallow flows*. John Wiley, 2001.

[10] R. LeVeque, "Finite Volume Methods for Hyperbolic Problems," *Cambridge University Press*, vol. 54, p. 258, 2002.

[11] C. M. Dafermos, *Hyperbolic Conservation Laws in Continuum Physics*, vol. 325. 2010.

[12] P. D. Lax, *Hyperbolic systems of conservation laws and the mathematical theory of shock waves*, vol. 11. SIAM, 1973.

[13] T.-P. Liu, "The deterministic version of the glimm scheme," *Communications in Mathematical Physics*, vol. 57, no. 2, pp. 135–148, 1977.

[14] P. Colella, "Glimm's method for gas dynamics," *SIAM Journal on Scientific and Statistical Computing*, vol. 3, no. 1, pp. 76–110, 1982.

[15] E. F. Toro, *Riemann Solvers and Numerical Methods for Fluid Dynamics: A Practical Introduction*. Springer, 1997.

[16] G. A. Sod, "A numerical study of a converging cylindrical shock," *Journal of fluid mechanics*, vol. 83, no. 04, pp. 785–794, 1977.

[17] L. Lobovskỳ, E. Botia-Vera, F. Castellana, J. Mas-Soler, and A. Souto-Iglesias, "Experimental investigation of dynamic pressure loads during dam break," *Journal of Fluids and Structures*, vol. 48, pp. 407–434, 2014.

[18] L. Delorme, A. Colagrossi, A. Souto-Iglesias, R. Zamora-Rodriguez, and E. Botia-Vera, "A set of canonical problems in sloshing, part i: Pressure field in forced roll—comparison between experimental results and sph," *Ocean Engineering*, vol. 36, no. 2, pp. 168–178, 2009.

[19] A. Jazcilevich and V. Fuentes-Gea, "The conservative random choice method for the numerical solution of the advection equation," *Monthly weather review*, vol. 127, no. 10, pp. 2281–2292, 1999.

[20] Z. H. C. Hsiung, "Application of the flux difference splitting method to compute nonlinear shallow water flow on deck," *int. Workshop on Water Waves and Floating Bodies*, pp. 83–87, 1994.

[21] J. Dillingham and J. Falzarano, "Three Dimensional Numerical Simulation of Green Water on Deck," *Third International Conference on Stability of Ships and Ocean Vehicles*, pp. 57–64, 1986.

[22] T. Santos and C. Guedes Soares, "Investigation into the effects of shallow water on deck in ship motions," in *Proceedings of the 8th international conference on the stability of ships and ocean vehicles, Madrid, Spain*, pp. 81–96, 2003.

[23] E. Toro, "On glimm-related schemes for conservation laws," *Preprint MMU-9602, Department of Mathematics and Physics, Manchester Metropolitan University, UK*, 1996.

Aalto-ST 17/2015

ISBN 978-952-60-6580-9 (pdf)
ISSN-L 1799-4896
ISSN 1799-4896 (printed)
ISSN 1799-490X (pdf)

Aalto University
School of Engineering
Department of Applied Mechanics
www.aalto.fi